CHORUS. I. Cosmic HydrOgen Reionization Unveiled with Subaru: Overview

Akio K. Inoue [1,2,3,*] Satoshi Yamanaka [2,3] Masami Ouchi,[4,5,6]
Ikuru Iwata [4,7] Kazuhiro Shimasaku,[8,9] Yoshiaki Taniguchi,[10,11]
Tohru Nagao,[11] Nobunari Kashikawa,[8] Yoshiaki Ono,[5] Ken Mawatari,[3,5]
Takatoshi Shibuya,[12] Masao Hayashi [4] Hiroyuki Ikeda,[13] Haibin Zhang,[5,14]
Yongming Liang,[4,7,8] Chien-Hsiu Lee [15] Miftahul Hilmi,[5,8]
Satoshi Kikuta,[16] Haruka Kusakabe,[17] Hisanori Furusawa [4,7]
Tomoki Hayashino,[18] Masaru Kajisawa,[11] Yuichi Matsuda,[4,7]
Kimihiko Nakajima,[4] Rieko Momose,[8] Yuichi Harikane,[4,19] Tomoki Saito,[20]
Tadayuki Kodama,[21] Shotaro Kikuchihara [5,8] Masanori Iye,[4]
and Tomotsugu Goto[22]

[1]Department of Physics, School of Advanced Science and Engineering, Faculty of Science and Engineering, Waseda University, 3-4-1 Okubo, Shinjuku, Tokyo 169-8555, Japan
[2]Waseda Research Institute for Science and Engineering, Faculty of Science and Engineering, Waseda University, 3-4-1 Okubo, Shinjuku, Tokyo 169-8555, Japan
[3]Department of Environmental Science and Technology, Faculty of Design Technology, Osaka Sangyo University, 3-1-1 Nakagaito, Daito, Osaka 574-8530, Japan
[4]National Astronomical Observatory of Japan, 2-21-1 Osawa, Mitaka, Tokyo, 181-8588, Japan
[5]Institute for Cosmic Ray Research, The University of Tokyo, 5-1-5 Kashiwa-no-ha, Kashiwa, Chiba 277-8582, Japan
[6]Kavli Institute for the Physics and Mathematics of the Universe (Kavli IPMU), WPI, The University of Tokyo, 5-1-5 Kashiwanoha, Kashiwa, Chiba 277-8583, Japan
[7]Department of Astronomical Science, The Graduate University for Advanced Studies, SOKENDAI, 2-21-1 Osawa, Mitaka, Tokyo 181-8588, Japan
[8]Department of Astronomy, Graduate School of Science, The University of Tokyo, 7-3-1 Hongo, Bunkyo-ku, Tokyo 113-0033, Japan
[9]Research Center for the Early Universe, Graduate School of Science, The University of Tokyo, 7-3-1 Hongo, Bunkyo-ku, Tokyo 113-0033, Japan
[10]The Open University of Japan, 2-11 Wakaba, Mihama-ku, Chiba, Chiba 261-8586, Japan
[11]Research Center for Space and Cosmic Evolution, Ehime University, 2-5 Bunkyo-cho, Matsuyama, Ehime 790-8577, Japan
[12]Kitami Institute of Technology, 165 Koen-cho, Kitami, Hokkaido 090-8507, Japan
[13]National Institute of Technology, Wakayama College, 77 Noshima, Nada-cho, Gobo, Wakayama 644-0023, Japan
[14]Department of Astronomy, Tsinghua University, No. 1 Qinghuayuan, Beijing 100084, China
[15]NSF's National Optical-Infrared Astronomy Research Laboratory, Tucson, AZ 85719, USA
[16]Center for Computational Sciences, University of Tsukuba, 1-1-1 Tennodai, Tsukuba, Ibaraki 305-8577, Japan
[17]Observatoire de Genève, Université de Genève, 51 chemin de Pégase, 1290 Versoix, Switzerland
[18]Research Center for Neutrino Science, Tohoku University, Aramaki, Aoba-ku, Sendai 980-8578, Japan

[19]Department of Physics and Astronomy, University College London, Gower Street, London WC1E 6BT, UK

[20]Nishi-Harima Astronomical Observatory, Centre for Astronomy, University of Hyogo, 407-2 Nishigaichi, Sayo, Sayo-gun, Hyogo 679-5313, Japan

[21]Astronomical Institute, Tohoku University, 6-3 Aramaki, Aoba-ku, Sendai 980-8578, Japan

[22]Institute of Astronomy, National Tsing Hua University, 101 Section 2 Kuang Fu Road, Hsinchu 300, Taiwan, ROC

*E-mail: akinoue@aoni.waseda.jp

Abstract

To determine the dominant sources for cosmic reionization, the evolution history of the global ionizing fraction, and the topology of the ionized regions, we have conducted a deep imaging survey using four narrow-band (NB) and one intermediate-band (IB) filters on the Subaru/Hyper Suprime-Cam (HSC), called Cosmic HydrOgen Reionization Unveiled with Subaru (CHORUS). The central wavelengths and full-widths-at-half-maximum of the CHORUS filters are, respectively, 386.2 nm and 5.5 nm for *NB387*, 526.0 nm and 7.9 nm for *NB527*, 717.1 nm and 11.1 nm for *NB718*, 946.2 nm and 33.0 nm for *IB945*, and 971.2 nm and 11.2 nm for *NB973*. This combination, including *NB921* (921.5 nm and 13.5 nm) from the Subaru Strategic Program with HSC (HSC SSP), is carefully designed, as if they were playing a chorus, to observe multiple spectral features simultaneously, such as Lyman continuum, Lyα, C IV, and He II for $z = 2$–7. The observing field is the same as that of the deepest footprint of the HSC SSP in the COSMOS field and its effective area is about 1.6 deg^2. We present an overview of the CHORUS project, which includes descriptions of the filter design philosophy, observations and data reduction, multiband photometric catalogs, assessments of the imaging quality, measurements of the number counts, and example use cases for the data. All the imaging data, photometric catalogs, masked pixel images, data of limiting magnitudes and point spread functions, results of completeness simulations, and source number counts are publicly available through the HSC SSP database.

Key words: catalogs — dark ages, reionization, first stars — galaxies: high-redshift — surveys

1 Introduction

Understanding cosmic reionization is one of the most important objectives in observational cosmology. Measurements of the Thomson scattering optical depth of free electrons in the intergalactic medium (IGM) in the cosmic microwave background with the Wilkinson Microwave Anisotropy Probe and Planck satellites place the epoch of hydrogen reionization at $z \sim 10$ (Komatsu et al. 2011; Planck Collaboration 2018). The detection of the Gunn–Peterson trough in the spectra of quasars at $z > 6$ (e.g., Fan et al. 2006; Becker et al. 2007) and the decrement in the luminosity functions (LFs) of Lyα emitters (LAEs) at $z > 6$ (e.g., Kashikawa et al. 2006, 2011; Ouchi et al. 2010; Hu et al. 2010, 2019; Nakamura et al. 2011; Konno et al. 2014; Matthee et al. 2015; Santos et al. 2016; Konno et al. 2018; Itoh et al. 2018; Taylor et al. 2020) suggest a rapid increase

in the hydrogen neutral fraction, $x_{\rm H\,I}$, beyond $z = 6$. The $x_{\rm H\,I}$ measurements obtained so far still have a large scatter due to the small statistics and the systematic uncertainty in each measurement (e.g., Robertson et al. 2015; Greig & Mesinger 2017; Inoue et al. 2018; Finkelstein et al. 2019; Naidu et al. 2020). New $x_{\rm H\,I}$ measurements near $z \sim 7$ based on large samples of galaxies over large cosmic volumes are required to reach a concordance in the history of reionization.

Galaxies such as LAEs and Lyman break galaxies (LBGs) at $z > 6$ can be the dominant ionizing sources if their Lyman continuum (LyC) emissivity or escape fraction $f_{\rm esc}$ is sufficiently high. The required $f_{\rm esc}$ is $\sim$20%, assuming a standard population synthesis model (e.g., Inoue et al. 2006; Robertson et al. 2015; Finkelstein et al. 2019; Naidu et al. 2020). Measuring the LyC emissivity of these galaxies,

which is still quite uncertain, is the most critical step in determining the ionization sources for reionization. Bright quasars do not contribute much to the LyC emissivity for reionization owing to their rarity (e.g., Bianchi et al. 2001), whereas faint active galactic nuclei (AGNs) might contribute to or even dominate (Giallongo et al. 2015; Madau & Haardt 2015). However, other observations suggest that faint AGNs are not sufficiently abundant (Kashikawa et al. 2015; Onoue et al. 2017; Matsuoka et al. 2018; Parsa et al. 2018). Measuring the LyC emissivity of AGNs is also required to resolve their role in reionization (Micheva et al. 2017; Grazian et al. 2018). The metal-free stellar population, the so-called Population III (Pop III) stars (e.g., Carlberg 1981), can be an important ionizing source, particularly in the early phase of the reionization process (e.g., Sokasian et al. 2004). Because their characteristics, such as the initial mass function (IMF), are unknown observationally owing to the lack of information (Nagao et al. 2005, 2008; Kashikawa et al. 2012; Vanzella et al. 2020), identifying Pop III clusters and revealing their nature are highly relevant to understanding their role in reionization.

Depending on the dominant ionizing source, the topology of reionization is expected to be different: "inside-out" (Iliev et al. 2006) by galaxies or "outside-in" (Miralda-Escudé et al. 2000) by X-ray sources, such as AGNs. Observationally, the spatial inhomogeneity of $x_{\rm HI}$ at $z \sim 6$ has been reported to be based on quasar spectra (Becker et al. 2015) and LAE LFs (Ouchi et al. 2010; Nakamura et al. 2011). Obtaining the overdensities of LAEs at $z \gtrsim 6.5$ may support the concept that these LAEs are located in the ionized bubbles produced by the galaxy overdensities (e.g., Castellano et al. 2016; Bagley et al. 2017; Higuchi et al. 2019; Harikane et al. 2019; Tilvi et al. 2020). Resolving the ionization topology is one of the main scientific goals for future H I 21 cm tomography with the Square Kilometer Array (SKA; e.g., Hasegawa et al. 2016). However, with a sufficiently large survey of LAEs and LBGs, we may visualize the $x_{\rm HI}$ map before the SKA era. Such topology observations will be important consistency checks of the ionizing source observations, by comparing the observed topology with the prediction based on the identified dominant ionizing sources.

The Hyper Suprime-Cam (HSC; Miyazaki et al. 2018; Komiyama et al. 2018; Kawanomoto et al. 2018; Furusawa et al. 2018) has the *widest* field of view (FoV), 1.75 deg^2, of an 8 m-class telescope. This unique capability, with a well-considered set of narrow-band (NB) filters, for the first time allows dealing with the central questions of reionization by an unprecedented wide and deep NB survey. Since 2007 we have studied the specifications of HSC NBs carefully (see section 2) and developed them under strict scientific reviews with the financial support of approximately 100 M

yen from the Japan Society for the Promotion of Science. Four of the NBs (*NB387*, *NB816*, *NB921*, and *NB101*) are included in the ongoing HSC Subaru Strategic Program (SSP; Aihara et al. 2018a) for deep surveys of LAEs at $z \simeq 2.2$, 5.7, 6.6, and 7.3 (Ouchi et al. 2018). The latter three high-z surveys provide new estimates of the cosmic average of $x_{\rm HI}$ at $z \simeq 6.6$ and 7.3 from comparison with LAE LFs (Ouchi et al. 2018; Shibuya et al. 2018a, 2018b; Konno et al. 2018; Inoue et al. 2018). However, the HSC SSP cannot address the LyC emissivity and the $x_{\rm HI}$ topology directly.

Thus, we initiated a Subaru intensive program, Cosmic HydrOgen Reionization Unveiled with Subaru (CHORUS), with *NB387*, *NB527*, *NB718*, *IB945*, and *NB973* (table 1; see figure 1). Supplying the data of the *NB921* and broad-band (BB) filters from the HSC SSP, we aim to answer the questions of the ionization source and the topology, in addition to the history, by measuring the LyC emissivity values of galaxies and AGNs, abundance of Pop III stars, and LF of faint AGNs, and visualizing the $x_{\rm HI}$ map directly (see subsections 6.1–6.5 for more information). These measurements are realized only in combination with our NBs. This program will become a legacy survey at least for a decade because no other deep and wide-area survey, such as the Large Synoptic Survey Telescope, has a set of NBs like this program.

This paper presents an overview of the CHORUS project and its first public data release, CHORUS PDR1. In section 2 we describe the CHORUS filter set in detail. Section 3 is a summary of the observations, data reduction, and photometric catalogs of the CHORUS data. Section 4 presents a summary of the imaging quality, such as the size of the point spread function and the limiting magnitude of each NB. In section 5, the number counts in the five CHORUS NBs are given as a set of fundamental measurements of the NB imaging data. Section 6 gives brief instructions on the usage of the CHORUS PDR1 data and some example science cases. A summary is found in the final section.

We assume a standard set of cosmological parameters, $H_0 = 70\,{\rm km\,s^{-1}\,Mpc^{-1}}$, $\Omega_M = 0.3$, and $\Omega_\Lambda = 0.7$, and use the AB magnitude system (Oke 1990) throughout the study.

2 Filter set

The CHORUS filter set consists of four NBs (*NB387*, *NB527*, *NB718*, and *NB973*) and one IB (*IB945*) in addition to *NB921* from HSC SSP. Table 1 is a summary of the characteristics of the filters, the targeted spectral features of high-z galaxies, and the redshift ranges. Figure 1

Table 1. Summary of filter properties.

Filter	Area-weighted mean (central position)			Redshift range of targeted features§				Papers using the NBs.‖
	CW*	FWHM†	TP‡	LyC	Lyα	C IV	He II	
NB387	386.2 (385.8)	5.5 (5.7)	0.842 (0.871)	>3.27	2.15–2.20	—	—	A18a, L20
NB527	526.0 (525.5)	7.9 (7.5)	0.956 (0.922)	>4.81	3.29–3.36	—	2.18–2.23	H20
NB718	717.1 (716.8)	11.1 (11.1)	0.927 (0.911)	—	4.85–4.94	—	3.34–3.41	Z20, H20
NB921♯	921.5 (920.4)	13.5 (13.4)	0.935 (0.937)	—	6.52–6.64	4.90–4.99	—	A18a, O18, H20
IB945	946.2 (944.7)	33.0 (32.2)	0.955 (0.952)	—	6.65–6.92	—	—	
NB973	971.2 (969.9)	11.2 (11.0)	0.878 (0.834)	—	6.94–7.04	—	4.88–4.95	I18, H20

*The central wavelength (CW) of the transmission function in units of nm.

†The full width at half maximum (FWHM) of the transmission function in units of nm.

‡The transmission peak (TP) of the transmission function itself (i.e., not including the instrumental and atmospheric throughput).

§(CW±FWHM/2)/λ − 1. Adopted rest-frame wavelength (λ) of the features: Lyman limit, 91.175 nm; Lyα, 121.567 nm; C IV, 154.949 nm; He II, 164.033 nm.

‖References: A18a, Aihara et al. (2018a); L20, Liang et al. (2020); H20, Hayashi et al. (2020); Z20, Zhang et al. (2020); O18, Ouchi et al. (2018); I18, Itoh et al. (2018)

♯The imaging data collected and presented in SILVERRUSH (Ouchi et al. 2018) of the HSC SSP (Aihara et al. 2018a).

shows the total efficiency of the NBs as well as HSC BBs.[1] The CHORUS filter set not only covers a wide redshift range of $2 \lesssim z \lesssim 7$ of Lyα but also enables us to observe multiple spectral features at specific redshifts at the same time. As found in figure 1, the LyC and He II 1640 line for $z \simeq 3.3$ LAEs selected with NB527 can be observed with NB387 and NB718, and similarly, the LyC, C IV line, and He II line for $z \simeq 4.9$ LAEs selected with NB718 can be observed with NB527, NB921, and NB973. For $z \simeq 2.2$ LAEs selected with NB387, the He II line can be observed with NB527 (see table 1). The last CHORUS filter, IB945, is a filter to select LBGs within a redshift range similar to that of LAEs selected with NB921 ($z \simeq 6.6$) and NB973 ($z \simeq 7.0$; see subsection 6.4 for its science case). It is also useful to trace the line-free continuum between the C IV and He II lines at $z \simeq 4.9$ (see figure 1). In the following, we further describe the philosophy of the HSC SSP and CHORUS filter specifications and the characteristics of the CHORUS filters measured in the laboratory.

The NB filter set for the HSC imaging survey was designed very carefully (Ouchi et al. 2018). The filter wavelengths in the redder wavelength range were determined to pass through OH sky windows at 816, 921, 973, and 1010 nm. The three filters, except for the one at 973 nm, were used for the NB imaging observations in the HSC SSP survey (Aihara et al. 2018a) called SILVERRUSH (Ouchi et al. 2018). The remaining NB973 filter became
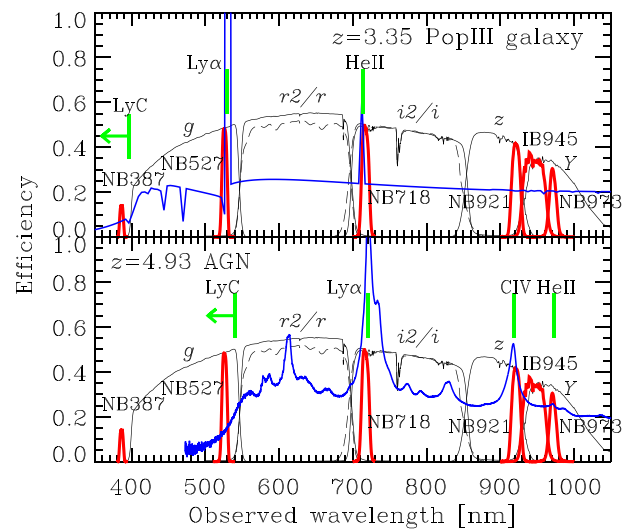

Fig. 1. Filter efficiency functions (narrow-band and broad-band are shown in red and black, respectively) with example spectra of a galaxy at $z = 3.35$ (top) and an AGN at $z = 4.93$ (bottom). For the $r2/r$ and $i2/i$ bands, the solid lines show the $r2$ and $i2$ transmissions and the dashed lines show the r and i transmissions. The effects considered in addition to the filter transmission are as follows: atmospheric transmission at the summit of Mauna Kea (airmass of 1.2 and water vapor column of 1.6 mm), the primary mirror reflectance, and the instrumental throughput of the HSC including the CCD quantum efficiency and an average vignetting effect in the field of view. (Color online)

a CHORUS filter. The filter wavelengths in the blue wavelength range were determined to ensure that multiple spectral features of the LAEs selected by an NB filter were captured by the other NB filters, and that strong rest-frame optical emission lines of the LAEs passed through the OH sky windows in the near-infrared range maximally. The selected wavelengths were 387, 527, and 718 nm, which

---

[1] In the UD COSMOS field of the HSC SSP, there are two filters each for the r and i bands, namely $r2/r$ and $i2/i$ (Kawanomoto et al. 2018). The newer $r2$ and $i2$ filters were used for about 60% of the data according to the HSC PDR2 web page ⟨https://hsc-release.mtk.nao.ac.jp/doc/index.php/data-2/⟩. These two filter images were all combined to make final coadd images of the r and i bands (Aihara et al. 2019).

Table 2. Summary of CHORUS observations and data qualities.

Filter	Observation dates	Exposure* [h]	PSF FWHM[†] [″]	5σ depth[‡] [AB] $\phi1.''5$	5σ depth[‡] [AB] $\phi2.''0$	Area[§] [deg^2]
NB387	2018 Jan 17, 18, 19	21/17.3	1.01 (0.99)	25.80[‖] (26.07)[‖]	25.42[‖] (25.65)[‖]	1.561
NB527	2017 Dec 16, 17, 18; 2018 Mar 15, 16, 18	10.5/8.9	0.83 (0.82)	26.72 (26.87)	26.30 (26.46)	1.613
NB718	2017 Feb 25, Mar 23, 25	13.5/7.7	0.69 (0.68)	26.29 (26.47)	25.87 (26.06)	1.575
IB945	2018 Dec 1, 2, 3, 12	10.2/10.2	0.62 (0.61)	25.77 (25.92)	25.36 (25.49)	1.558
NB973	2017 Jan 26, 28	15/14.7	0.64 (0.64)	25.19 (25.37)	24.79 (24.96)	1.603

*On-source exposure time/effective exposure time for the final coadd image, except for `patches` at the edge of the field of view, where these times are somewhat shorter due to dithering.

[†]FWHM of the point spread function (PSF): the area-weighted average value (the value in the central `patch` 404).

[‡]A 5σ limiting magnitude for circular apertures of 1.''5 or 2.''0 in diameter: the area-weighted average value (the value in the central `patch` 404).

[§]Effective area after removing masked regions.

[‖]Value corrected for zero-point offset (-0.45 mag). See the explanation in the last paragraph of section 3.

became the CHORUS filters.[2] This combination allows us to observe LyC, Lyα, and He II at $2 \lesssim z \lesssim 5$ as described above. The [O II] 3727 and Hα lines for $z \simeq 2.2$ LAEs selected with *NB387* fall in the OH sky windows at 1.19 and 2.10 μm. The [O III] 4959/5007 for $z \simeq 3.3$ LAEs selected with *NB527* are also observable at 2.15/2.17 μm in the middle of the K band.

The full width at half maximum (FWHM) of each filter was also determined carefully (Ouchi et al. 2018). The FWHM of *NB921* was determined first, to cover the full width of the OH sky window. The FWHMs of the other NB filters, except for *NB973* and *IB945*, were subsequently determined to ensure the same efficiency for Lyα line detection as *NB921*. Because the observed equivalent width of a line is $EW_{obs} = (1 + z)EW_0$, where EW_0 is the intrinsic equivalent width and z is the source redshift, the FWHMs were determined by the relation $FWHM = FWHM_{921} \times (1 + z)/(1 + 6.58)$. Note that 6.58 is the redshift of the LAEs selected with *NB921*. *NB973* has a narrower FWHM than the relation to enhance the efficiency of the Lyα line detection and compensate for the shallower depth in the band. *IB945* has an FWHM to fill the wavelength gap between *NB921* and *NB973*.

The HSC filter is 600 mm in diameter, making it a challenging task to realize a uniform multilayer interferometric coating to produce narrow bandpass filters with sharp cut-on and cut-off wavelengths. Therefore, there was a small deviation from the specifications during the production process. We examined the performance of the NB filters produced by the manufacturers, Optical Coatings Japan (*NB387*, *NB527*, *NB718*, *NB921*, and *NB973*) and Materion (*IB945*), using the method described in Kawanomoto et al. (2018). Slight non-uniformities in the central

wavelength (CW), FWHM, and transmission peak (TP) were found along the radial direction. The CW tended to increase with the radius, except for *NB387* where the CW variation was more complex. The FWHM also tended to increase in the outer part, except for *NB387* where it decreased with the radius. The overall CW variation was less than 0.3%–0.5% (the worst case was found in *NB527*), whereas the FWHM variation ranged from a few percent to 10% (*NB387*). The TP also tended to increase with the radius, except for *NB387* again, where the TP decreased with the radius. The overall TP variation was less than 1%–10% (*NB973*). A higher degree of uniformity was found in the azimuthal direction. Table 1 presents the CWs, FWHMs, and TPs for the area-weighted mean transmission functions of the CHORUS filters. The values for the transmission functions at the center positions of the filters are also provided for reference. The machine-readable filter transmission curves are available at the Subaru/HSC website.[3]

3 Observations, data reduction, and photometric catalogs

We were awarded 13 nights in the classical mode of the Subaru Telescope for four consecutive semesters from S16B to S18A (i.e., 2 yr) under a Subaru open-use intensive program, S16B-001I (PI: A. K. Inoue). We were also awarded 11.5 h in the queue mode in semester S18B under an open-use normal program, S18B-004 (PI: A. K. Inoue), to supplement the time loss due to the weather during the original four semesters. Under the two programs, we performed deep imaging observations using our NB filters on the HSC on the dates listed in table 2. The on-source exposure time, as well as the effective exposure time used for the final coadd images, are also listed in table 2. Some of the

[2] Although *NB387* was also used for the "Deep" layer observations in the HSC SSP (Aihara et al. 2018a; Ouchi et al. 2018), there was no data taken in the footprint of the "UltraDeep" layer in the COSMOS field, where the CHORUS observations were performed.
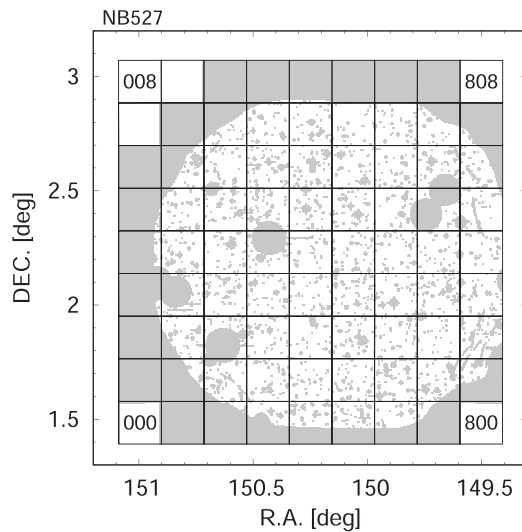
[3] ⟨https://subarutelescope.org/Observing/Instruments/HSC/sensitivity.html⟩.

Fig. 2. Masked area (gray shade) in the *NB527* image as an example. HSC SSP UD COSMOS, `tract` 9813, is divided into 9 × 9 `patches` as indicated by the lattice; the `patch` numbers are indicated at the four corners.

observation dates were not under photometric conditions (i.e., low transparency), and we discarded a fraction of the observed data owing to bad quality. The observing field was the COSMOS field (Scoville et al. 2007), which has the same footprint as the HSC SSP Ultra Deep (UD) layer (Aihara et al. 2018a). Any sky region in the HSC SSP survey is defined by a set of two numbers, `tract` and `patch` (Aihara et al. 2018b). Most of the HSC SSP UD COSMOS is covered by `tract` number 9813. There are 9 × 9 sub-regions (`patches`) in a `tract`. Each `patch` has a sky area of $12' \times 12'$, and a `tract` has an area of $1°\!\!.8 \times 1°\!\!.8$. The `patch` numbers are expressed as 000 (south-east corner), 001, 002, ..., 008 (north-east corner), 100, 101, ..., 800 (north-west corner). The `patch` configuration in the UD COSMOS `tract` 9813 is shown in figure 2.

The data reduction was conducted using the HSC SSP pipeline, `hscPipe` version 6.7, which is also used for the SSP PDR2 data processing. We used the obtained imaging data satisfying the following conditions:

- exposure time 1200 s, seeing $< 1''\!\!.5$, and transparency >0.4 for *NB387*
- exposure time 1200 s (but three frames of 468–1016 s), seeing $< 1''\!\!.2$, and transparency >0.75 for *NB527*
- exposure time 1200 s, seeing $< 1''\!\!.2$, and transparency >0.76 for *NB718*
- exposure time 1200 s, seeing $< 1''\!\!.2$, and transparency >0.9 for *NB973*
- exposure time 720 s, seeing $< 1''\!\!.2$, and transparency >0.7 for *IB945*.

The `hscPipe` pipeline generates several multiband photometric catalogs, which we call the "CHORUS PDR1 catalog." Source detection is based on the signal-to-noise ratio

(S/N) within the PSF against the background noise fluctuation (Bosch et al. 2018) and the detection criterion is $5\,\sigma$, as in the SSP PDR papers (Aihara et al. 2018b, 2019). The reader should refer to the pipeline paper (Bosch et al. 2018) and the SSP PDR2 paper (Aihara et al. 2019) for the detailed procedures for data reduction, source detection, and photometry. In the following we describe some specific points for the CHORUS data release.

The photometric zero-points for the CHORUS NBs were determined based on the BB photometry of the Galactic stars in the Pan-STARRS1 (PS1) catalog (Chambers et al. 2016), similar to the method for the HSC SSP (Aihara et al. 2018b, 2019). The color terms translating PS1 BB magnitudes to HSC NB magnitudes were estimated based on the Pickles stellar spectral templates (Pickles 1998). This seems to work well, except for *NB387*, where a systematic zero-point offset was found in Liang et al. (2020)— see also the last paragraph in this section. The multiband photometry was conducted with the so-called *priority order* (Bosch et al. 2018) of the filters, which was defined as *i*, *r*, *z*, *y*, *g* for the BB filters, followed by the order of *NB921*, *NB816*, *NB973*, *NB718*, *NB527*, *NB1010*, *NB387*, and *IB945* for the NB filters. The priority order of the filters was used to determine the object positions.[4] For line emitters detected in a single NB image but not detected in any other BB and NB images, photometry on the NB image was conducted at the positions of the detections in the NB image. However, for line emitters that were also detected in other BB (and NB) images, the photometry positions were forced to be the positions in the most prioritized band among the images in which the objects were detected. In such cases, photometry on the NB image, which includes the line flux, can be underestimated if there are spatial offsets between the prioritized band and NB positions. This would not be a problem for bright objects that are detected well both in the prioritized band and NB images; however, it might be an issue for objects that are marginally detected in the prioritized band and whose positions in the band have a large uncertainty. Quantifying this effect would need a large set of pipeline simulations that was reserved for future line emitter analyses.

There are several different photometric magnitudes in the CHORUS PDR1 multiband catalog. In this paper we do not recommend using `cmodel` magnitudes, which represent the total flux densities obtained by the brightness profile fitting (Bosch et al. 2018) and were considered representative magnitudes in SSP PDR1 (Aihara et al. 2018b). This

---

[4] This is the so-called *forced* catalog based on multiband photometry at the positions in the most prioritized band. The `hscPipe` pipeline makes another catalog based on photometry at the positions in each band separately, called the *meas* (or unforced) catalog (Aihara et al. 2018b). We do not deal with the *meas* catalog in this paper because the photometry may not give reliable colors owing to potentially different positions in different bands.

is because there is an issue of erroneously bright `cmodel` magnitudes for some objects in SSP PDR2; see Aihara et al. (2019), and the follow-up study by Hayashi et al. (2020). According to sub-subsection 6.6.3 of the SSP PDR2 paper (Aihara et al. 2019), this problem is likely to be caused by a failure in the deblending procedure in crowded regions of objects. This problem can be severe in the HSC SSP UD footprint in the COSMOS field, where the CHORUS observations were performed, because the very deep BB depth yields a very high density of detected objects.

We instead recommend using the `undeblended_convolvedflux` magnitudes for estimates of total magnitudes.[5] These measurements are based on the aperture magnitudes of the final coadd images smoothed with a Gaussian function (see subsection 3.6 of the SSP PDR1 paper, Aihara et al. 2018b). The Gaussian smoothing size is defined as the resultant FWHM of the point sources in the smoothed images, which is $0\rlap{.}''59$, $0\rlap{.}''84$, $1\rlap{.}''1$, or $1\rlap{.}''3$ (Aihara et al. 2019). This process produces a set of smoothed BB and NB images with the same selected PSF FWHM. Subsequently, the flux densities of each object in all the smoothed (i.e., PSF-matched) images are measured in a circular aperture of diameter size $1\rlap{.}''1$, $1\rlap{.}''5$, $2\rlap{.}''0$, or Kron-size, and aperture corrections are also applied assuming a point source.[6] This process is performed for all the detected objects as a function of `hscPipe` (Aihara et al. 2018b, 2019). These PSF-matched magnitudes yield better colors in crowded fields (Aihara et al. 2018b), which is the most important feature to reliably select LAEs in two-color diagrams. This procedure is very similar to the method performed in previous studies with `SExtractor` (Bertin & Arnouts 1996). In this study, we adopt $1\rlap{.}''5$ ($2\rlap{.}''0$) diameter apertures on $0\rlap{.}''84$ ($1\rlap{.}''1$) smoothed images.[7]

There are two significant known issues in the SSP PDR2 photometric catalog (Aihara et al. 2019), and they are also present in the CHORUS PDR1 catalog similarly produced by `hscPipe` 6.7. The first one is that the uncertainties of the PSF-matched magnitudes are underestimated (see sub-subsection 5.8.11 of the SSP PDR1 paper, Aihara et al. 2018b). This occurs because covariances are introduced by the Gaussian smoothing process. This problem persists in the SSP PDR2 release (Aihara et al. 2019). Therefore, we do not recommend using these cataloged values of uncertainties for the PSF-matched magnitudes. Instead, we estimated the uncertainties by measuring the rms values of the aperture flux densities in the actual images. The limiting magnitudes provided in the next section are based on these measurements.[8] The second issue is that there is a systematic offset in the zero-point of *NB387* in the SSP PDR2 release (Aihara et al. 2019). This is due to the metallicity effect of the 4000 Å break in stellar spectra on $NB387 - g$ color. The `hscPipe` pipeline uses the Pickles spectral templates based on Solar metallicity stars (Pickles 1998) for zero-point estimations. However, the actual stars used for the calibration seem to be dominated by metal-poor halo stars because these stars are faint ($g \sim 20$) and the HSC survey fields are located in high Galactic latitudes. This template mismatch causes a systematic offset of the zero-point only for *NB387*. A complete description and full analyses are found in the appendix of Liang et al. (2020). We did not correct the *NB387* magnitudes in the CHORUS PDR1 catalog, but recommend that users apply a 0.45 mag subtraction correction to the *NB387* magnitudes in the catalog, as recommended by the HSC SSP team.[9]

4 Imaging data quality

4.1 Definition of masked areas

We defined the masked areas in each CHORUS NB image based on the flags from `hscPipe` and the visual inspection conducted by one of the authors. Figure 2 shows the masked area of the *NB527* image as an example. Pixels in each image that satisfied the following conditions for the `hscPipe` flags were selected as masked pixels: `pixelflags_bright_object` is True (pixels affected by bright objects) or `pixelflags_saturatedcenter` is True (pixels affected by count saturation). In addition to these pixels, we also masked out the pixels affected by the halos of bright stars. Generally, these halos are more prominent in NB images than in BB images, probably due to the multilayer interferometric thin film coating of the NBs. We supplementarily set larger circular (sometimes elliptical) masks to cover these bright stars' halos if the pixels with the above flags do not cover sufficiently large areas. One of the authors (S.Y.) selected these pixels by eye. The edge of the FoV was also defined by eye by the same author to avoid lower-S/N

---

[5] There is another similar measurement called `convolvedflux`, for which the source deblender algorithm in `hscPipe` works. On the other hand, the source deblending process was turned off for `undeblended_convolvedflux`. We have found that the two magnitudes of `undeblended_convolvedflux` and `convolvedflux` are identical in most cases.

[6] The amount of aperture correction can be found as `undeblended_convolvedflux_X_Y_apcorr` in the catalog database, where X and Y are the numbers indicating the target convolution size and the aperture size, respectively.

[7] If the native PSF of a band is larger than the target smoothing FWHM, any Gaussian smoothing is not applied to the band and the native images are used for the aperture photometry (see subsection 3.6 of Aihara et al. 2018b). Such a case happened for *NB387* in the $0\rlap{.}''84$ target FWHM smoothing.

[8] The uncertainty in a magnitude is given by $\delta m = (2.5/\ln 10)/(S/N)$. The S/N of each object can be estimated from the ratio of `undeblended_apertureflux` in the catalog database to the 1σ aperture flux density calculated from the limiting magnitudes in the next section.

[9] ⟨https://hsc-release.mtk.nao.ac.jp/doc/index.php/known-problems-2/#hsc-link-10⟩.

regions. The effective survey area of each NB was calculated from the total number of non-masked pixels in the image, and is listed in table 2. The exact positions of the masked pixels are available as image files in a FITS format.

4.2 Sizes of point spread functions

We measured a representative FWHM of the PSF in each `patch` of the CHORUS NB images using `SExtractor`[10] version 2.19.5 (Bertin & Arnouts 1996). We adopted the median of the `FWHM_IMAGE` measured by `SExtractor` for stellar-like objects not in the masked areas as the representative FWHM of the PSF. Stellar-like objects were selected depending on the measurements of `SExtractor` as those satisfying the following three criteria: (1) `MAG_AUTO` in the range $[18.0, 22.0]$ for $NB387$ and $NB527$, $[18.0, 21.0]$ for $NB718$ and $NB973$, and $[19.0, 21.0]$ for $IB945$; (2) `ELONGATION` <1.2 (i.e., nearly circular shape); and (3) `FLAG` < 4 (i.e., not located in a bad position, such as saturated or truncated pixels; for details, see Bertin & Arnouts 1996). If there were an insufficient number of stellar-like objects in a `patch` because of an extremely small non-masked area, we did not measure the FWHM of the PSF. The measured FWHMs and their spatial variations are shown in figure 3, and the values of the area-weighted average and the central `patch`, 404, are listed in table 2. The FWHM values range from $1''$ to $0''.6$, depending on the band. The spatial variation in the FWHM values in each NB is as small as $<0''.02$, demonstrating the excellent stability of the image quality across the entire FoV of the HSC.

4.3 Limiting magnitudes

We measured the limiting magnitudes in each `patch` of the CHORUS NB images by conducting aperture photometry at random sky positions with the Python packages `Astropy`[11] and `photutils`. [12] A large number of random positions (10000 as default, and 5000 or 1000 at the edge of the FoV depending on the available area) were prepared in each `patch` by avoiding the masked pixels and the pixels of the objects detected by `SExtractor` in advance. If the non-masked area in a `patch` was less than 1 arcmin^2, we did not measure the limiting magnitudes. For convenience, we measured the limiting magnitudes with two aperture sizes ($1''.5$ and $2''.0$ in diameter) in each `patch` of each CHORUS NB image. We estimated the background brightness locally by adopting a median count in an annulus of $1''.5$ ($2''.0$) width and $2''.5$ ($3''.0$) inner diameter set around the $1''.5$ ($2''.0$) aperture and subtracted it from the aperture count as a correction for the background contribution. The

standard deviation, σ, was obtained from the histogram of the background-subtracted aperture counts by fitting a Gaussian function. Note that we did not apply any aperture correction to the counts. The 5σ values of the area-weighted average and those in the central `patch`, 404, for the two aperture sizes are listed in table 2. The spatial variation in the 5σ values for the $1''.5$-diameter aperture case are shown in figure 4. We can see a radial dependence of the limiting magnitudes; it is ~ 1 mag shallower at the outer edge compared to the center. The `patch` 403 shows a shallower depth than the radial trend, which was also reported by Hayashi et al. (2020). This is probably because half of the four channels in a CCD chip (SDO-ID=0_20/DET-ID=33) close to the `patch` center have been unavailable since 2016 November–December (see the CCD information page of HSC on the Subaru Telescope website)[13] and the dithering amount was too small to compensate the low-sensitivity area.

4.4 Completeness

We estimated the detection completeness based on a simulation of embedding and recovering numerous mock galaxies in actual CHORUS NB images using `hscPipe`, `Astropy`, and `GALSIM` (Rowe et al. 2015).[14] These mock galaxies were assumed to have an intrinsic brightness profile described by a circular Sérsic profile with index $n = 1.5$ and a half-light radius of 1 pix of the HSC images ($0''.17$). The adopted radius corresponds to 1.4–0.9 physical kiloparsecs for $2 < z < 7$ and is very consistent with those of typical LBGs/LAEs (Shibuya et al. 2015; Kawamata et al. 2018). When embedding the mock galaxies into each `patch` image, we convoluted the brightness profile with the PSF of the image. Because the intrinsic sizes of the mock galaxies were very small compared to the PSF size, the embedded profiles were similar to the PSF but slightly extended. The locations at which to embed the mock galaxies were chosen randomly, not avoiding the actual objects, to consider cases in which the extended and bright galaxies overlap and hide faint ones. We considered nine intrinsic magnitudes of mock galaxies in a range of ± 2.0 mag, with a 0.5 mag step around the 5σ limiting magnitude. The number of input mock galaxies was 500 for each intrinsic magnitude in each `patch` of each band. We ran `hscPipe` to detect the mock galaxies and measure the magnitudes. The criteria for successful recovery were detection within a radius of $0''.5$ from the embedded location and a magnitude difference of less than 0.5 mag. We adopted the `undeblended_convolvedflux` magnitude ($0''.84$ FWHM convolution and $\phi 1''.5$ aperture case, except for $NB387$, where $1''.1$ FWHM convolution and $\phi 2''.0$ aperture case was adopted) as the output

---

[10] ⟨http://www.astromatic.net/software/sextractor⟩.

[11] ⟨https://www.astropy.org/⟩.

[12] ⟨https://photutils.readthedocs.io/en/stable/⟩.

[13] ⟨https://www.naoj.org/Observing/Instruments/HSC/ccd.html⟩.

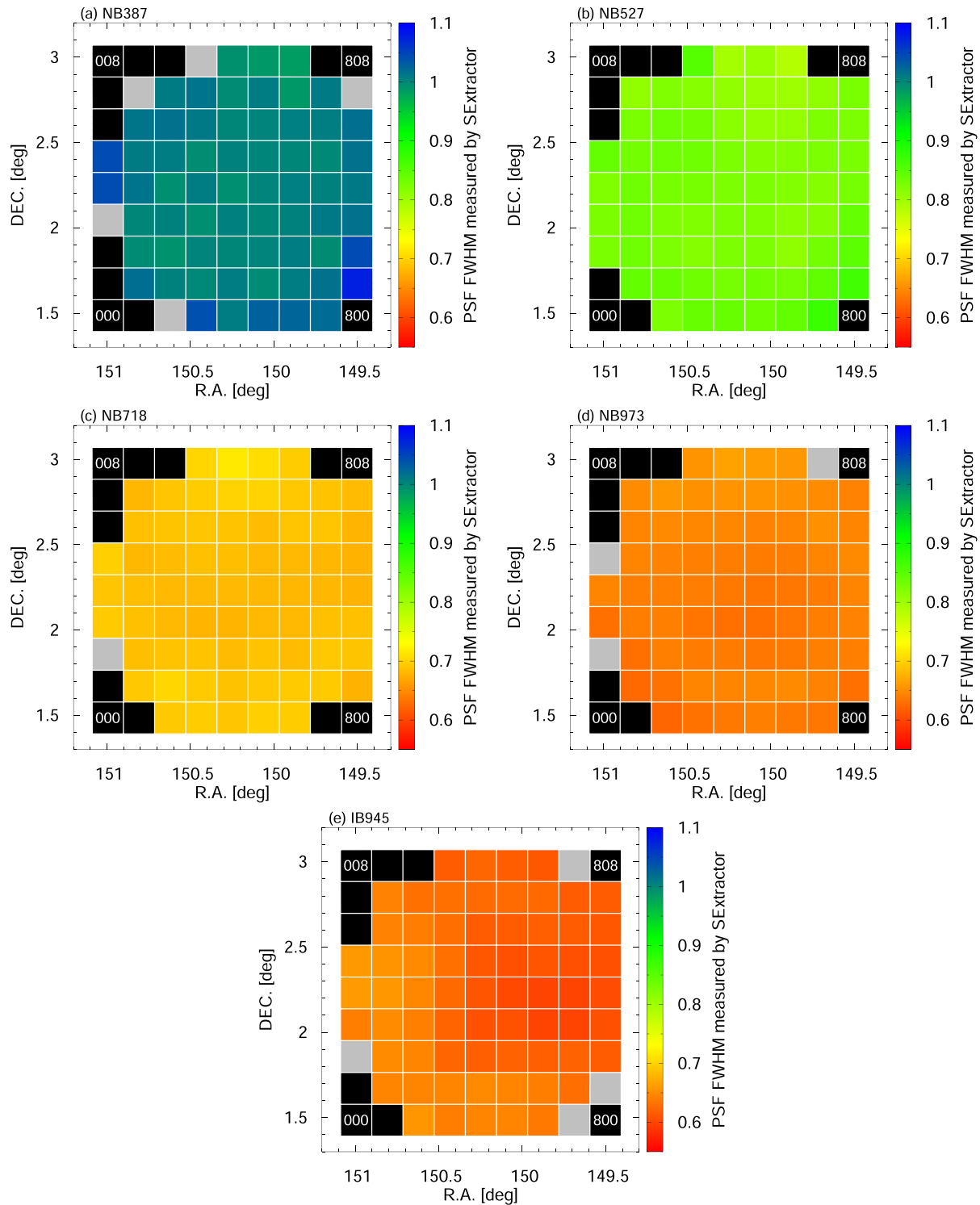[14] ⟨https://github.com/GalSim-developers/GalSim⟩.

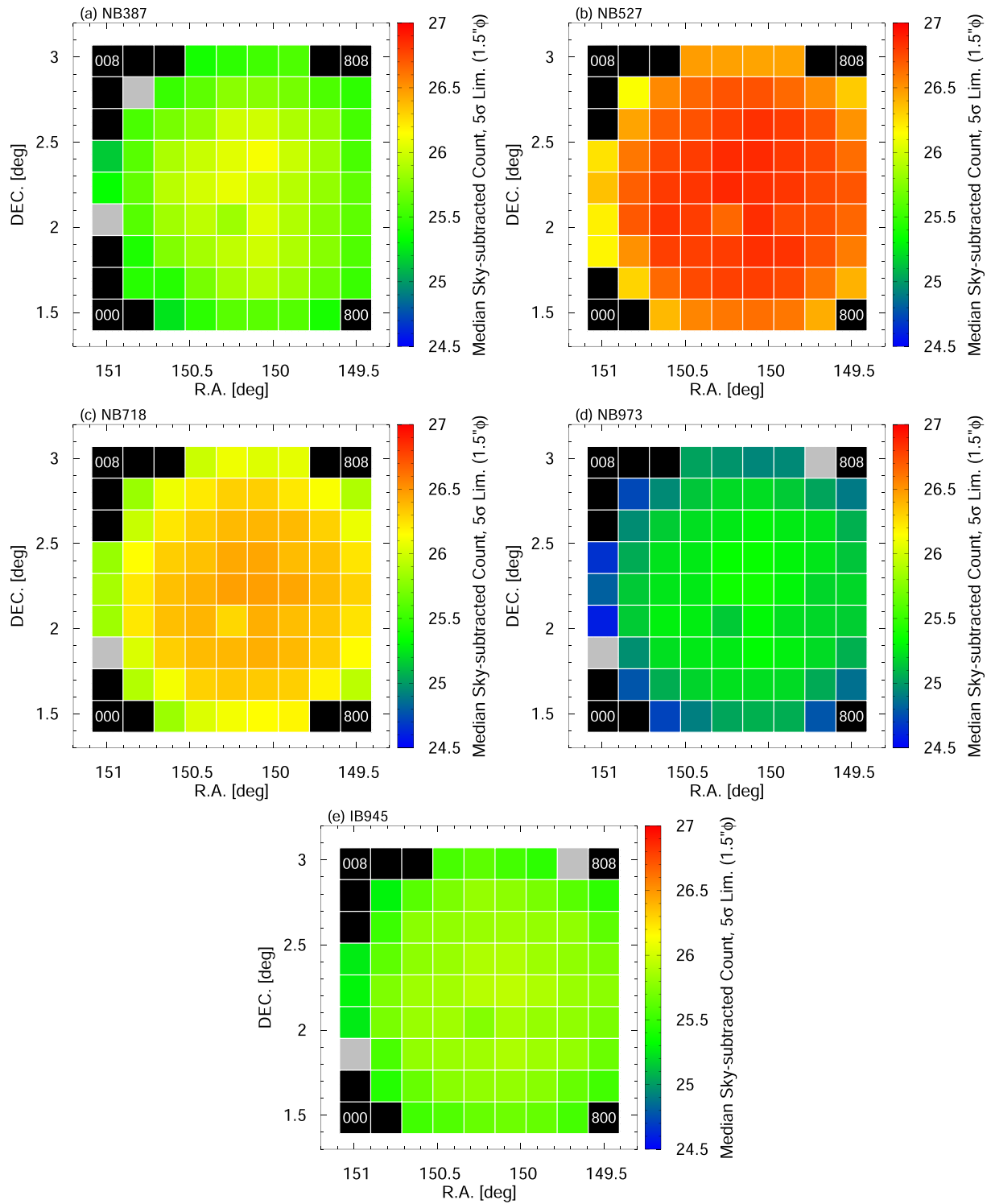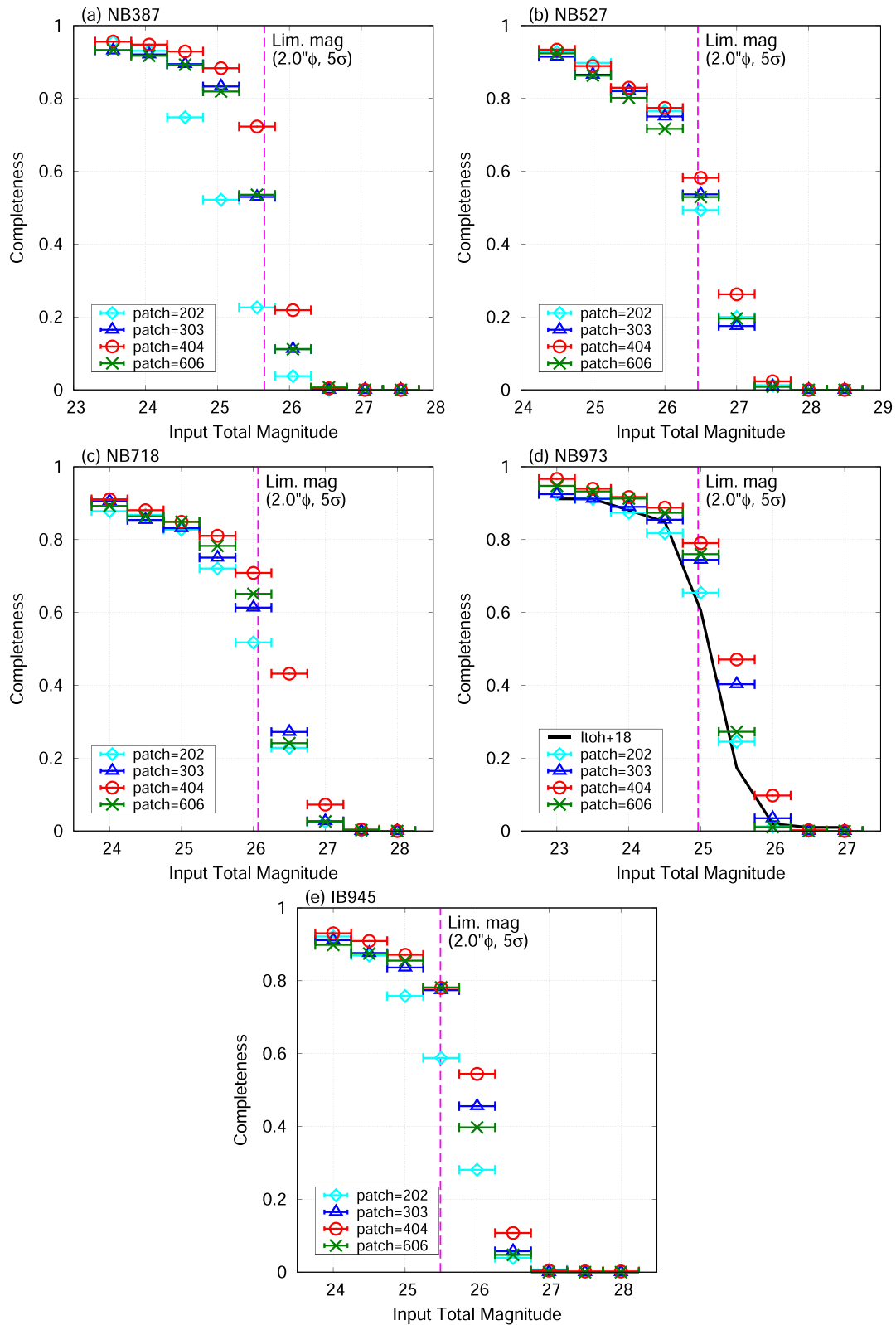**Fig. 3.** FWHMs of PSF and their spatial variation for *NB387* (top left), *NB527* (top right), *NB718* (middle left), *NB973* (middle right), and *IB945* (bottom). The black areas indicate `patches` that have no effective area, and the gray areas indicate `patches` where there are an insufficient number of stars for PSF FWHM measurement owing to the small effective area. (Color online)

total magnitude for figure 5; however, the results with the `convolvedflux` magnitude were essentially the same. Note that the `undeblended_convolvedflux` and `convolvedflux` magnitudes are aperture-corrected by a PSF model and

equivalent to the total magnitude for the point sources. The detection completeness is defined as the ratio of the number of successfully recovered galaxies to the number of embedded mock galaxies. The mock galaxies placed in the

Fig. 4. Five-σ limiting magnitudes and their spatial variation for *NB387* (top left), *NB527* (top right), *NB718* (middle left), *NB973* (middle right), and *IB945* (bottom). The black areas indicate `patches` that have no effective area, and the gray areas indicate `patches` where there are insufficient non-masked pixels for limiting magnitude measurements. The aperture size is 1.″5 in diameter. (Color online)

masked areas were excluded from the analysis in this final step. To moderate the computation time, we conducted this experiment just the four `patches` 202, 303, 404, and 606, instead of all 81 `patches`.

Figure 5 shows the results of the simulations of the detection completeness. We find that the completeness is $\gtrsim 60\%$ at the 5 σ limiting magnitude ($\phi 2.″0$ not aperture-corrected) in each `patch`, which is reasonable. Even at magnitudes

Fig. 5. Detection completeness of *NB387* (top left), *NB527* (top right), *NB718* (middle left), *NB973* (middle right), and *IB945* (bottom). The cyan, blue, red, and green points with error bars denote the results for `patch`es 202, 303, 404, and 606, respectively. For *NB973*, the black solid line indicates the result of Itoh et al. (2018). We also display the 5σ limiting magnitudes measured with a $2''.0$-diameter aperture (not total magnitudes) in `patch` 404 by the vertical magenta dashed line in each panel. These results were obtained with `undeblended_convolvedflux` magnitudes; however, essentially the same results are obtained with `convolvedflux` magnitudes. (Color online)

brighter than the limiting magnitudes, the completeness is only 80%–95% and does not reach 100% because of the hiding effect by bright objects. For *NB527*, the completeness is relatively lower than that of the other bands. This seems to be caused by source confusion due to the very deep depth with a moderate PSF size. Indeed, the surface number density of the detected objects in *NB527* up to a 5σ limit of 26.46 AB ($\phi 2\rlap{.}{''}0$) corresponds to an areal fraction of $\sim$13% even if we assume a circular area with a radius equal to the PSF FWHM size ($r = 0\rlap{.}{''}82$) per object. For *NB973*, we also present the average completeness over all the `patches` estimated similarly but independently by Itoh et al. (2018); it is slightly lower than ours but is broadly consistent. Actually, Itoh et al. (2018) used `hscPipe` version 4.0.5, and their 5σ-limiting magnitude in the $1\rlap{.}{''}5$-diameter aperture of 25.0 was 0.4 mag shallower than that of this study.

5 Number counts

To verify the CHORUS PDR1 catalog we calculated the source number counts in the CHORUS NBs and compared the results with those reported in the literature. We adopted the `undeblended_convolvedflux` magnitudes ($0\rlap{.}{''}84$ FWHM convolution and $\phi 1\rlap{.}{''}5$ aperture case, except for *NB387*, where $1\rlap{.}{''}1$ FWHM convolution and $\phi 2\rlap{.}{''}0$ aperture case was adopted) as the total magnitude of the objects, and excluded the objects and area in the masked regions. The total magnitudes for each object were corrected for Galactic extinction using the values listed in the CHORUS PDR1 catalog, which are estimated from Schlegel, Finkbeiner, and Davis (1998) dust maps (see also the HSC SSP PDR papers Aihara et al. 2018b, 2019). These extinction magnitudes are small, for instance $\sim$0.1 mag even in *NB387* in which the extinction effect is the severest. We also applied a catalog flag, `forced.merge_peak_XXXX` is `True`, where XXXX = n387, n527, n718, i945, or n973, to ensure that we count only the sources detected in the NB that we are considering. Otherwise, the number count included the sources that were not actually detected in the NB because `hscPipe` lists all the sources detected in any single band in the catalogs. Because the BB images of the HSC SSP are deeper than the CHORUS NB images, numerous faint BB sources, which are not detected in any of the CHORUS NBs, are also listed in the CHORUS PDR1 catalog.

Figure 6 shows the number count measurements. We only present the data points for those magnitudes at which the completeness (see figure 5) is larger than 10%. We also display the literature data of both BBs and NBs whose wavelengths are close to those of each NB. There are excellent agreements between all the CHORUS number counts and the literature data. For example, the number counts

of *NB718*, *NB973*, and *IB945* present excellent agreement with the data of Subaru/Suprime-Cam: *i* from Kashikawa et al. (2004) for *NB718*, and *z* from Kashikawa et al. (2004) and *NB921* from Ouchi et al. (2010) for *NB973* and *IB945*. The *NB527* number count also agrees with those of Subaru/Suprim-eCam *NB503* from Ouchi et al. (2008) and *V* from Kashikawa et al. (2004); however, there are slight differences from those in bluer bands, like *B* from Kashikawa et al. (2004) and *NB497* from Yamada et al. (2012). Because the slopes of the number counts reported in the literature are steeper at shorter wavelengths, the CHORUS results seem to follow this trend. For *NB387* after zero-point correction (see section 3), the number count data agree with those of Suprime-Cam/*NB387* from Nakajima et al. (2012), Suprime-Cam/*B* from Kashikawa et al. (2004), and CFHT/MegaCam/*u* from Sawicki et al. (2019) at magnitudes fainter than 22. At brighter magnitudes, the two *NB387* data Suprime-Cam's lie between the two BB literature data, which is reasonable given the trend mentioned above, because the wavelength of *NB387* is indeed between those of the *B* and *u* bands. The zero-point uncorrected *NB387* number count is less than those reported in the literature data. These results suggest the necessity and validity of the zero-point correction.

6 How to use the catalog and example use cases for the CHORUS data

The CHORUS PDR1 catalog is available at the Catalog Archive Server (CAS)[15] of the HSC-SSP. An example SQL query to obtain a list of the coordinates, `patch`, the Galactic extinction in *NB387*, $\phi 2\rlap{.}{''}0$ aperture *NB387* magnitudes, *NB387* total magnitudes (`undeblended_convolvedflux` with $1\rlap{.}{''}1$ FWHM convolution and $\phi 2\rlap{.}{''}0$ aperture), and the corresponding aperture corrections for the sources detected in *NB387* is as follows:

```
SELECT
    object_id, ra, dec, patch, a_n387
    n387_undeblended_apertureflux_20_mag
    n387_undeblended_convolvedflux_2_20_mag
    n387_undeblended_convolvedflux_2_20_apcorr
FROM
    s18a_chorus.forced
    LEFT JOIN s18a_chorus.forced3 USING (object_id)
    LEFT JOIN s18a_chorus.forced6 USING (object_id)
WHERE
    tractSearch(forced.object_id, 9813)
    AND forced.nchild = 0
    AND forced.detect_ispatchinner IS True
    AND forced.merge_peak_n387 IS True
```

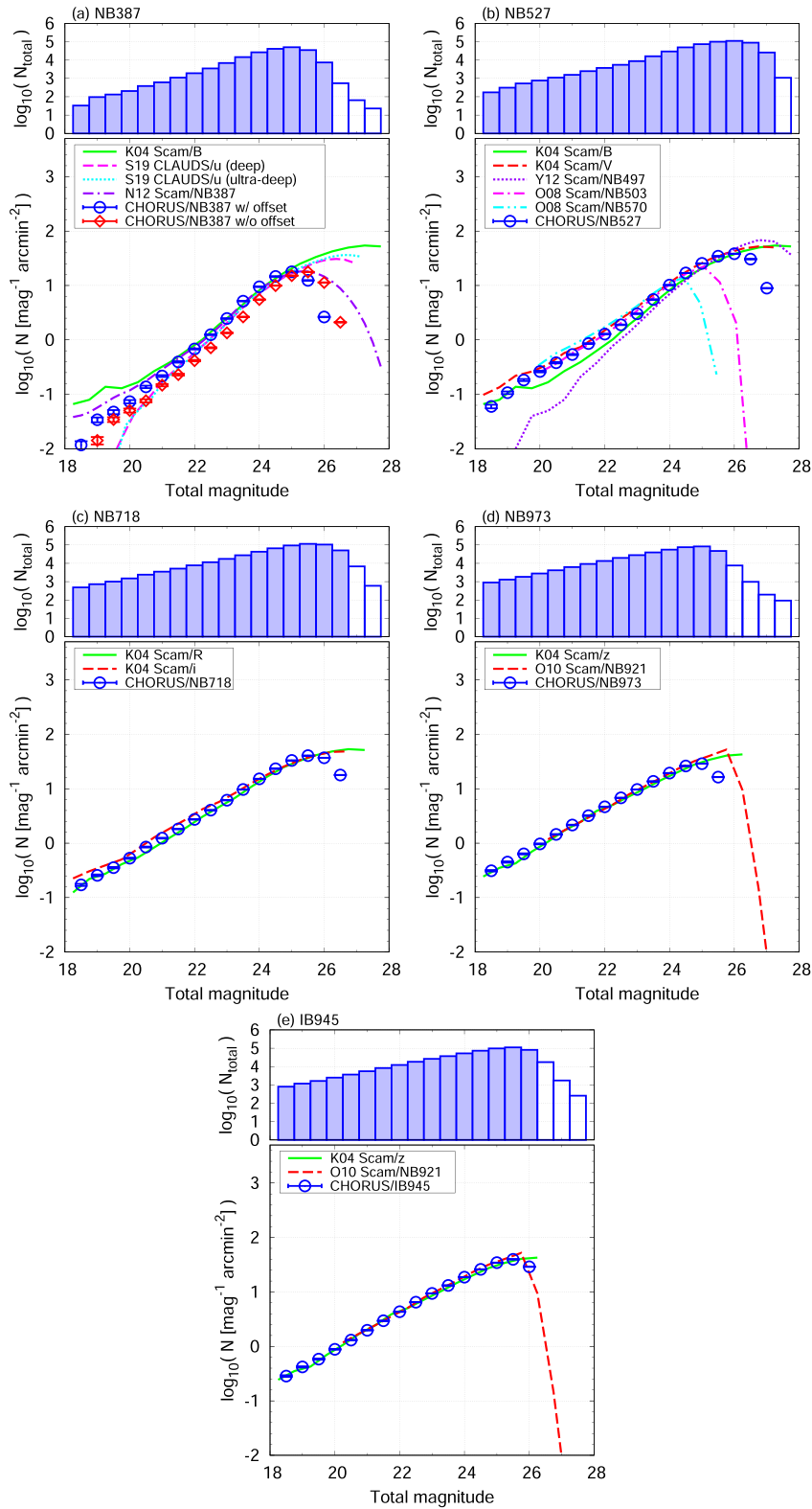[15] ⟨https://hsc-release.mtk.nao.ac.jp/datasearch/⟩.

Fig. 6. Source number counts for *NB387* (top left), *NB527* (top middle), *NB718* (top right), *NB973* (bottom left), and *IB945* (bottom right). For each band, the upper panel shows a histogram of the actual numbers of detected sources and the bottom panel shows the number density per magnitude per square arcminutes. An empty histogram indicates a magnitude range where detection completeness is less than ∼10% and the probability of spurious detections may be high. Number counts taken from the literature are also shown in each panel for comparison. For *NB387*, we show number counts both with and without zero-point correction for catalog magnitudes produced by `hscPipe` version 6.7. References of literature data: K04, Kashikawa et al. (2004); O08, Ouchi et al. (2008); O10, Ouchi et al. (2010); Y12, Yamada et al. (2012); N12, Nakajima et al. (2012); S19, Sawicki et al. (2019). (Color online)

```
AND forced.n387_pixelflags_saturatedcenter IS
    False
AND forced.n387_pixelflags_bright_object IS
    False
```

The CHORUS PDR1 (*forced*) catalog consists of seven files: s18a_chorus.forced, s18a_chorus.forced2, ..., s18a_chorus.forced7. The FITS files of the masked areas (figure 2), spatial maps of PSF sizes (figure 3) and limiting magnitudes (figure 4), numerical data of detection completeness simulations (figure 5), and numerical data of measured number counts (figure 6) are also available through the website.[16]

In the following, we describe four specific ongoing studies using the CHORUS data, and other ancillary studies including results published so far.

6.1 Lyman continuum survey of galaxies and AGNs

In the CHORUS project we perform a LyC survey for galaxies and AGNs at $z \simeq 3.3$ and 4.9 using *NB387* and *NB527*, respectively (see figure 1). The samples are mainly the LAEs selected by *NB527* ($z \simeq 3.3$) and *NB718* ($z \simeq 4.9$). An *average* LyC-to-UV flux density ratio, or f_{esc}, for the LAEs will be estimated by stacking analysis. Combining the LyC-to-UV ratios corrected for IGM transmission and the observed UV luminosity densities, we can estimate the LyC luminosity densities and examine whether galaxies dominate the LyC emissivity at $z \sim 3$–5. We can also detect the LyC from individual LAEs and AGNs. The number of such LyC galaxies at $z > 3$ is still limited (e.g., Iwata et al. 2009, 2019; Vanzella et al. 2012, 2015; Steidel et al. 2018). This program will increase that number significantly. Follow-up spectroscopy of these reliable LyC galaxies allows f_{esc} calibration from the non-ionizing properties, such as a high [O III]/[O II] ratio (Nakajima & Ouchi 2014; de Barros et al. 2016; Nakajima et al. 2020). Once we establish the relation between the LyC emissivity (or f_{esc}) values and the properties of galaxies observable at longer wavelengths at $z \lesssim 5$, we can estimate f_{esc} for the galaxies in the epoch of reionization ($z > 6$). In this epoch, direct LyC observations are impossible owing to the severe absorption caused by the neutral hydrogen atoms in the IGM (Inoue & Iwata 2008; Inoue et al. 2014).

6.2 Surveys of faint AGNs as dual emitters

Using *NB718* and *NB921*, we can select a population of faint AGNs at $z \simeq 4.9$ as Lyα–C IV dual emitters if we appropriately treat the effects of broad lines whose line widths are broader than the NB widths (figure 1). This selection method is unique because these faint AGNs with a magnitude range similar to that discussed by Giallongo et al. (2015) are difficult to isolate from the LBGs by any combination of BB colors. Moreover, our *NB527* data allows the direct measurement of the LyC of these faint AGNs. The faint-AGN population reported by Giallongo et al. (2015) can reproduce the LyC emissivity required to keep the Universe ionized at $z \sim 5$–6 if $f_{esc} = 1$ (Madau & Haardt 2015). We examine if this is the case not only by measuring the faint-AGN LF but also by measuring the f_{esc} of this population. Simultaneously, we measure f_{esc} of galaxies at the same redshift and study their contribution directly. Subsequently, we identify the population that dominates the cosmic LyC emissivity at $z \sim 3$–5 and infer the source of the cosmic reionization at $z > 6$.

6.3 Surveys of Pop III-dominated galaxies

Population III stars are expected to have high LyC emissivity and may play a significant role in the early phase of reionization (e.g., Sokasian et al. 2004). However, observational evidence for this stellar population is still inconclusive (e.g., Kashikawa et al. 2012; Rydberg et al. 2015; Vanzella et al. 2020), and their characteristics, e.g., the initial mass function and the LyC emissivity, are unknown. Theoretically, Pop III star clusters can be formed even at $z \sim 2$–3, depending on the efficiency of the IGM metal enrichment (e.g., Tornatore et al. 2007; Johnson 2010; de Souza et al. 2011). Indeed, pristine ($Z < 10^{-4}$) gas clouds, from which Pop III stars may form, are found at $z \simeq 3$ (e.g., Fumagalli et al. 2011). Identifying the epoch of the termination of metal-free star formation is also a very important problem. The He II emission line can be an indicator of Pop III stars (e.g., Tumlinson et al. 2001; Schaerer 2003). Using our well-tuned set of NBs, we can search for Lyα–He II dual emitters at $z \simeq 2.2$, 3.3, and 4.9 (see table 1 and figure 1). Such a dual emitter search was performed by Nagao et al. (2008) with the Suprime-Cam for $z \sim 4$. We update the upper limit on the He II line luminosity density or the Pop III star formation rate density by Nagao et al. (2008) with a seven times larger area and up to ~ 1 mag deeper imaging data at a wider redshift range of $z = 2$–5. This will enable us to constrain the metal-enrichment efficiency in the IGM more strongly than before.

6.4 Mapping spatial distributions of ionized bubbles

Because Lyα photons are sensitive to x_{HI}, the distribution of the LAEs depends on both x_{HI} and the large-scale structure (LSS). However, LBGs are selected by the continuum and

---

[16] ⟨https://hsc-release.mtk.nao.ac.jp/doc/index.php/chorus/⟩.

are not very sensitive to $x_{\rm HI}$ but simply trace the LSS. If we normalize the number density of the LAEs for each location by that of the LBGs, we can isolate the spatial distribution of $x_{\rm HI}$; we can visualize the $x_{\rm HI}$ map directly from the LAE-to-LBG density ratio. An essential point is to select LBGs with a similar redshift to the NB-selected LAEs whose redshift variation is as small as $\Delta z \simeq 0.1$. Although such an LBG selection is not feasible by BB filters, we can reach $\Delta z \simeq 0.3$ using an intermediate filter, *IB945* for redshifts around $z = 6.6$ and 7.0. From the spatial variation of the observed number density ratio, *we can visualize an $x_{\rm HI}$ map far ahead of the future 21 cm experiments, such as the SKA.* Such an $x_{\rm HI}$ mapping opens a new pathway to examine the ionization topology, for example allowing measurements of the ionized bubble size directly.

6.5 Ancillary sciences

Very wide ($1.6\,\rm deg^2$) and very deep ($\gtrsim 0.1\,L_*$) LAE samples at $z \simeq 2.2$, 3.3, 4.9, 6.8, and 7.0 are obtained by this program. An LAE LF at $z = 7.0$ has already been published as CHORUS paper II (Itoh et al. 2018), reporting a very similar LF shape to those at $z = 5.7$ and 6.6 with a small overall decrement compared to the lower-z ones. This indicates that the reionization process does not alter the shape of the LAE LF, in contrast to a previous claim of a bright-end hump (Zheng et al. 2017). A comprehensive LAE search in the CHORUS data in conjunction with the HSC SSP data is ongoing, adopting a machine learning technique (Y. Ono et al. in preparation). A study of intensity mapping of Lyα emission is also ongoing (S. Kikuchihara et al. in preparation). More LAE-related studies, including environmental ones and optical emission line properties in the near-infrared band, are also ongoing. We are also searching for spatially extended LAEs (Lyα blobs) in the imaging data. The results of a Lyα blob survey at $4.9 \leq z \leq 7.0$ has been published recently as CHORUS paper III (Zhang et al. 2020), which reports a Lyα blob at $z \simeq 7.0$, the highest-z blob found so far. [O II], [O III], Hβ, and Hα emitters at various redshifts are also studied with the CHORUS data in conjunction with the HSC SSP data (Hayashi et al. 2020) and Spitzer data (Harikane et al. 2018). More line emitter studies, including AGN surveys, will be performed in future. The CHORUS PDR1 data will be useful for various studies performed all over the world. We strongly encourage readers' own studies using the dataset.

7 Summary

In this study we conducted a deep imaging survey using a set of narrow-band and intermediate-band filters, named Cosmic HydrOgen Reionization Unveiled with Subaru (CHORUS), with the Hyper Suprime-Cam equipped on the Subaru Telescope. The filter set used in the survey is shown in figure 1. The wavelengths, *NB387*, *NB527*, *NB718*, *NB973*, and *IB945*, summarized in table 1, were chosen in a very well-organized manner to maximize the scientific outcomes when the filters were used in combination with another NB, *NB921*, from the Subaru Strategic Program for HSC. The observations were performed on 18 nights during the period from 2017 January to 2018 December in an intensive program of the Subaru Telescope. The observing field was the COSMOS field (Scoville et al. 2007). The data reduction, source detection, and multi-band photometry were conducted using `hscPipe`, the official pipeline software for the HSC developed by the HSC SSP team (Bosch et al. 2018). The `hscPipe` version used was 6.7, the same as that used for HSC SSP public data release 2 (Aihara et al. 2019). Because there is a known problem for the `cmodel` magnitudes in this version, we recommended using the `undeblended_convolvedflux` magnitudes instead. The imaging data qualities were examined thoroughly in a spatially dependent manner, as shown in figures 3 and 4. For each NB/IB, typical values of the size of point spread functions, $5\,\sigma$ limiting magnitude, and survey area excluding the carefully defined masked regions (see figure 2 as an example) are summarized in table 2. An extensive set of mock observation simulations was performed to estimate the source detection completeness, as shown in figure 5. We checked the source number counts and compared them with previous studies, as shown in figure 6. Excellent agreement with the literature data was obtained in each NB/IB. All the images and photometric catalogs are publicly available through the HSC SSP database. This data release is called CHORUS PDR 1.

References

Aihara, H., et al. 2018a, PASJ, 70, S4
Aihara, H., et al. 2018b, PASJ, 70, S8
Aihara, H., et al. 2019, PASJ, 71, 114
Bagley, M. B., et al. 2017, ApJ, 837, 11
Becker, G. D., Bolton, J. S., Madau, P., Pettini, M., Ryan-Weber, E. V., & Venemans, B. P. 2015, MNRAS, 447, 3402
Becker, G. D., Rauch, M., & Sargent, W. L. W. 2007, ApJ, 662, 72
Bertin, E., & Arnouts, S. 1996, A&AS, 117, 393
Bianchi, S., Cristiani, S., & Kim, T.-S. 2001, A&A, 376, 1
Bosch, J., et al. 2018, PASJ, 70, S5

Carlberg, R. G. 1981, MNRAS, 197, 1021
Castellano, M., et al. 2016, ApJ, 818, L3
Chambers, K. C., et al. 2016, arXiv:1612.05560
de Barros, S., et al. 2016, A&A, 585, A51
de Souza, R. S., Yoshida, N., & Ioka, K. 2011, A&A, 533, A32
Fan, X., et al. 2006, AJ, 132, 117
Finkelstein, S. L., et al. 2019, ApJ, 879, 36
Fumagalli, M., O'Meara, J. M., & Prochaska, J. X. 2011, Science, 334, 1245
Furusawa, H., et al. 2018, PASJ, 70, S3
Giallongo, E., et al. 2015, A&A, 578, A83
Grazian, A., et al. 2018, A&A, 613, A44
Greig, B., & Mesinger, A. 2017, MNRAS, 465, 4838
Harikane, Y., et al. 2018, ApJ, 859, 84
Harikane, Y., et al. 2019, ApJ, 883, 142
Hasegawa, K., et al. 2016, arXiv:1603.01961
Hayashi, M., et al. 2020, PASJ, 72, 86
Higuchi, R., et al. 2019, ApJ, 879, 28
Hu, E. M., Cowie, L. L., Barger, A. J., Capak, P., Kakazu, Y., & Trouille, L. 2010, ApJ, 725, 394
Hu, W., et al. 2019, ApJ, 886, 90
Iliev, I. T., Mellema, G., Pen, U.-L., Merz, H., Shapiro, P. R., & Alvarez, M. A. 2006, MNRAS, 369, 1625
Inoue, A. K., et al. 2018, PASJ, 70, 55
Inoue, A. K., & Iwata, I. 2008, MNRAS, 387, 1681
Inoue, A. K., Iwata, I., & Deharveng, J.-M. 2006, MNRAS, 371, L1
Inoue, A. K., Shimizu, I., Iwata, I., & Tanaka, M. 2014, MNRAS, 442, 1805
Itoh, R., et al. 2018, ApJ, 867, 46
Iwata, I., et al. 2009, ApJ, 692, 1287
Iwata, I., Inoue, A. K., Micheva, G., Matsuda, Y., & Yamada, T. 2019, MNRAS, 488, 5671
Johnson, J. L. 2010, MNRAS, 404, 1425
Kashikawa, N., et al. 2004, PASJ, 56, 1011
Kashikawa, N., et al. 2006, ApJ, 648, 7
Kashikawa, N., et al. 2011, ApJ, 734, 119
Kashikawa, N., et al. 2012, ApJ, 761, 85
Kashikawa, N., et al. 2015, ApJ, 798, 28
Kawamata, R., Ishigaki, M., Shimasaku, K., Oguri, M., Ouchi, M., & Tanigawa, S. 2018, ApJ, 855, 4
Kawanomoto, S., et al. 2018, PASJ, 70, 66
Komatsu, E., et al. 2011, ApJS, 192, 18
Komiyama, Y., et al. 2018, PASJ, 70, S2
Konno, A., et al. 2014, ApJ, 797, 16
Konno, A., et al. 2018, PASJ, 70, S16
Liang, Y., et al. 2020, ApJ, submitted (arXiv:2008.01733)
Madau, P., & Haardt, F. 2015, ApJ, 813, L8
Matsuoka, Y., et al. 2018, ApJ, 869, 150
Matthee, J., Sobral, D., Santos, S., Röttgering, H., Darvish, B., & Mobasher, B. 2015, MNRAS, 451, 400
Micheva, G., Iwata, I., & Inoue, A. K. 2017, MNRAS, 465, 302
Miralda-Escudé, J., Haehnelt, M., & Rees, M. J. 2000, ApJ, 530, 1
Miyazaki, S., et al. 2018, PASJ, 70, S1
Nagao, T., et al. 2008, ApJ, 680, 100
Nagao, T., Motohara, K., Maiolino, R., Marconi, A., Taniguchi, Y., Aoki, K., Ajiki, M., & Shioya, Y. 2005, ApJ, 631, L5
Naidu, R. P., Tacchella, S., Mason, C. A., Bose, S., Oesch, P. A., & Conroy, C. 2020, ApJ, 892, 109
Nakajima, K., et al. 2012, ApJ, 745, 12

Nakajima, K., Ellis, R. S., Robertson, B. E., Tang, M., & Stark, D. P. 2020, ApJ, 889, 161

Nakajima, K., & Ouchi, M. 2014, MNRAS, 442, 900

Nakamura, E., Inoue, A. K., Hayashino, T., Horie, M., Kousai, K., Fujii, T., & Matsuda, Y. 2011, MNRAS, 412, 2579

Oke, J. B. 1990, AJ, 99, 1621

Onoue, M., et al. 2017, ApJ, 847, L15

Ouchi, M., et al. 2008, ApJS, 176, 301

Ouchi, M., et al. 2010, ApJ, 723, 869

Ouchi, M., et al. 2018, PASJ, 70, S13

Parsa, S., Dunlop, J. S., & McLure, R. J. 2018, MNRAS, 474, 2904

Pickles, A. J. 1998, PASP, 110, 863

Planck Collaboration 2020, A&A, 641, A6

Robertson, B. E., Ellis, R. S., Furlanetto, S. R., & Dunlop, J. S. 2015, ApJ, 802, L19

Rowe, B. T. P., et al. 2015, Astron. Comput., 10, 121

Rydberg, C.-E., et al. 2015, ApJ, 804, 13

Santos, S., Sobral, D., & Matthee, J. 2016, MNRAS, 463, 1678

Sawicki, M., et al. 2019, MNRAS, 489, 5202

Schaerer, D. 2003, A&A, 397, 527

Schlegel, D. J., Finkbeiner, D. P., & Davis, M. 1998, ApJ, 500, 525

Scoville, N., et al. 2007, ApJS, 172, 1

Shibuya, T., et al. 2018a, PASJ, 70, S14

Shibuya, T., et al. 2018b, PASJ, 70, S15

Shibuya, T., Ouchi, M., & Harikane, Y. 2015, ApJS, 219, 15

Sokasian, A., Yoshida, N., Abel, T., Hernquist, L., & Springel, V. 2004, MNRAS, 350, 47

Steidel, C. C., Bogosavljević, M., Shapley, A. E., Reddy, N. A., Rudie, G. C., Pettini, M., Trainor, R. F., & Strom, A. L. 2018, ApJ, 869, 123

Taylor, A. J., Barger, A. J., Cowie, L. L., Hu, E. M., & Songaila, A. 2020, ApJ, 895, 132

Tilvi, V., et al. 2020, ApJ, 891, L10

Tornatore, L., Ferrara, A., & Schneider, R. 2007, MNRAS, 382, 945

Tumlinson, J., Giroux, M. L., & Shull, J. M. 2001, ApJ, 550, L1

Vanzella, E., et al. 2012, ApJ, 751, 70

Vanzella, E., et al. 2015, A&A, 576, A116

Vanzella, E., et al. 2020, MNRAS, 494, L81

Yamada, T., Nakamura, Y., Matsuda, Y., Hayashino, T., Yamauchi, R., Morimoto, N., Kousai, K., & Umemura, M. 2012, AJ, 143, 79

Zhang, H., et al. 2020, ApJ, 891, 177

Zheng, Z.-Y., et al. 2017, ApJ, 842, L22